energies

MDPI

Article

A Hybrid Experimental-Numerical Method to Support the Design of Multistage Pumps

Federico Fontana [1] and Massimo Masi [2,*]

[1] Franklin Electric srl—R&D, 36031 Dueville, Italy; federico.fontana@fele.com
[2] Department of Management and Engineering—DTG, University of Padova, 36100 Vicenza, Italy
* Correspondence: massimo.masi@unipd.it

Abstract: The paper uses a hydraulic performance analysis method to support the design of stock production multistage pumps. The method relies on a hybrid numerical–experimental approach conceived as a trade-off between accuracy and cost. It is based on CFD analyses incorporating experimental data of leakage flows across the sealing elements to obtain accurate predictions without the need of inclusion in the CFD model of small-scale features, which strongly increase the model complexity and computational effort. The aim of the paper is to present and validate this method. To this end, a 6-stage vertical pump manufactured by the stainless-steel metal-sheets-forming technique was considered as the benchmark. A series of experimental tests were performed to hydraulically characterize the impeller and return-channels-sealing elements by means of an "ad hoc" designed test rig. The characteristic curves of the sealing elements were embedded on the CFD model implemented in accordance with the strategy proposed in a previous authors' work to obtain satisfactory predictions of multistage pumps' hydraulic performance with minimum computational effort with the analytical correction of single-stage single-channel computations to account for the interaction between adjacent stages. To further explore the capabilities of the hybrid model, axial thrust measurements were performed by means of another "ad hoc" designed experimental apparatus. The application of the method to the benchmark pump shows that the hybrid model predicts the static head and efficiency with an error value lower than 1% at its best efficiency operation, and estimates the axial thrust with a 5% average error in the operating range from approximately 70% to 120% of the best efficiency duty.

Keywords: multistage pumps; hybrid experimental-CFD performance analysis; axial thrust prediction; axial thrust; sealing systems performance test rigs

Citation: Fontana, F.; Masi, M. A Hybrid Experimental-Numerical Method to Support the Design of Multistage Pumps. *Energies* **2023**, *16*, 4637. https://doi.org/10.3390/en16124637

Academic Editor: Helena M. Ramos

Received: 17 April 2023
Revised: 1 June 2023
Accepted: 8 June 2023
Published: 11 June 2023

1. Introduction

General background. The low cost of today's computational resources and the advancements in turbulence modelling have made the computational-fluid-dynamics (CFD) Reynolds-averaged Navier–Stokes simulation (RANS) a standard tool for the study of hydraulic pumps. In particular, the 360-degree full-domain unsteady-RANS (U-RANS) simulations performed on million cell grids allow for reliable analyses of the internal flow features as well as rather accurate predictions of the global hydraulic performance parameters. This is confirmed, for example, by the comparison between the U-RANS computations recently documented by Sonawat et al. [1] and Capurso et al. [2]. The former authors obtained satisfactory agreement between the calculated and measured head curves, but a less accurate estimation of the efficiency, using approximately 1.5 million cells to simulate the entire operating range of a double-suction pump, whereas the latter also satisfactorily predicted the efficiency of a novel pump design with a crossed-vane impeller using approximately 10 million cells.

The problem to be solved. On the other hand, the cell numbers used in the two single-stage pump simulation examples mentioned above confirm that the CFD analysis of multistage pumps by means of full-domain U-RANS is still a computationally demanding task, which

becomes very challenging as the stage counts increase and, most times, is justified for manufacturers of stock production machines only as the very final assessment of a new design just before the prototype experimental testing activity.

Thus, many of the simplified approaches necessary in the past to analyse single-stage turbomachines with the limited computational resources available at that time (e.g., steady-state multi-reference-frame calculations and single-channel calculations) are still at present widely used for CFD calculations at both industrial and scientific levels.

Literature review. To overview the several modelling alternatives and the corresponding expected accuracy in the simulation of multistage pumps, without the need of discussing a vast of references, the focus is limited to the multi-stage pumps belonging to the "compact design" category, i.e., machines composed by a series of centrifugal-flow stages in which the flow exiting the impeller is collected in an annular chamber feeding centripetal-flow fixed vanes (hereafter, return channels). In fact, the literature dealing with CFD analyses of compact design multistage pumps is still not considerably abundant. A representative sample of the main features and prediction accuracy of the modelling approaches suggested by different authors to deal with the numerical analysis of this pump type is summarised in Table 1.

Table 1. Basic features of the alternative CFD approach to model "compact design" multistage pumps.

Ref. and Year	Stage Counts	CFD Domain			Grid Features			Models		Overall Accuracy	
		Stages	Vanes *	Type †	Cells [$\times 10^6$] All/for Vane	Cell Size ‡ [mm]	y+/Near-Wall Prism Layers	Turbulence	Motion ~	Head Mean/Max	Efficiency Mean/Max
[3] 2002	3	1	1	S	-/0.28	-	n.d./-	κ-ε	MFR	−4%/−25% [1] 12%/40% [2]	n.d. [1] n.d. [2]
[4] 2004	10	1	1	S	-/≈0.60	-	<10/-	κ-ε	TADS	<1%/- [3]	-/<+5% [3]
[5] 2006	4	1 [4]	all	S/U [5]	2.9/≈0.4	-	10–250/n.d.	κ-ε	MFR	+6% [6]	±3% [6]
[6] 2009	6	6	all	U	8/≈0.15	-	n.d./n.d.	κ-ε	MFR	−5% [6]	−2% [6]
[7] 2012	6	2	all	S	2.5/<0.07	2.9	30–100/-	κ-ε	MFR	+3% [6]	+1% [6]
[8] 2013	5	2	all	U	1.1/<0.07	2.9	30–50/0	κ-ε	MFR	+7% [6]	+8% [6]
[9] 2013	4	4	all	U	1/≈0.03	6.6	n.d./n.d.	κ-ε	MFR	+5% [6]	+2% [6]
[10] 2013	4	4	all	U	2.1/≈0.05	3.3	n.d./-	κ-ε RNG	MFR	n.d.	n.d.
[11] 2015	6	6	all	U	27/≈0.75	-	n.d./n.d.	κ-ω SST	MFR	+5%/+11%	+8%/+13%
[12] 2016	2	2	all	U [7]	3/≈0.25	1.90	100/4	κ-ε	MFR	±3%/-	±7%/-
[13] 2016	4	4 [4]	all	S	8/0.19	1.82	30–60/-	κ-ε	MFR	-/±1%	-/±3%
[14] 2016	6	1 [8]	1	S [9]	-/0.53	1.88	25–70/-	κ-ε	MFR	2%/<+5%	<4%/8%
[15] 2016	7	7	1	S	2/0.28	1.08	<30/-	κ-ω SST	MFR	-/<+15%	6%/8% [10]
[16] 2017	5	2 [4]	all	S	3.2/≈0.18	1.91	n.d./-	κ-ε	MFR	±3%/-	6%/20% [11]
[17] 2019	1.5	1.5	all	S	2/≈0.2	-	n.d./-	κ-ε	MFR	5%/- [10]	n.d.
[18] 2020	4	4 [12]	all	U [7]	3.9/≈0.16	1.45	<30/4 ally+	κ-ε R. [13]	MG	<5%/−7%	≈10%/n.d.
[19] 2021	3	3	all	S	7.3/≈0.35	1.81	n.d./-	κ-ω SST	MFR	5.77%/n.d.	n.d.
[20] 2022	2	2 [4]	all	S	3/≈0.38	5.59	n.d./-	κ-ω SST	MFR	3%/3% [14]	6%/6% [15]
[21] 2022	3	3	1	S	2.5/≈0.14	2.85	<100/-	κ-ω SST	MFR	5%/+16% [16]	6%/+16% [16]

* Passages for stage, i.e., impeller vanes and the corresponding return channel vanes. † S = structured; U = unstructured. ‡ Estimated, where possible, as: (impeller diameter)/(cell for vane counts) $^{1/3}$. ~ MFR = steady multi-reference frame; TADS = unsteady time-averaged domain scale; MG = unsteady moving grids. [1] Estimated for pump B from Figure 7.21 in [3]. [2] Estimated for pump D from Figure 7.22 in [3]. [3] Estimated from Figure 7 in [4]. [4] Sealings and side gaps are included. [5] Tetrahedral unstructured grids in the entire return channels region. [6] Best efficiency point only. [7] Polyhedral grids. [8] Side gaps and correction for pre-rotation are included. [9] Triangular prisms grid only in the first one-third of the return channel (see Figure 1c). [10] Against catalogue data. [11] Estimated from Figure 7 in [16]. [12] Side gaps. [13] Realizable plus two-layer model. [14] Estimated from Figure 22c in [20]. [15] Estimated from Figure 22a in [20]. [16] Estimated from Figure 6 in [21].

From the analysis of the table, it is apparent that most of the references used steady-state RANS calculations and overestimated the pump head and efficiency (see the positive percentage errors in the last two columns), especially at flow rates higher than the best efficiency duty. The standard κ-ε is generally chosen as the turbulence closure model. Some of the authors (e.g., [4,13]) compared the predictions of several two-equation turbulence models and obtained the better accuracy using the standard version of either the κ-ε or κ-ω closure.

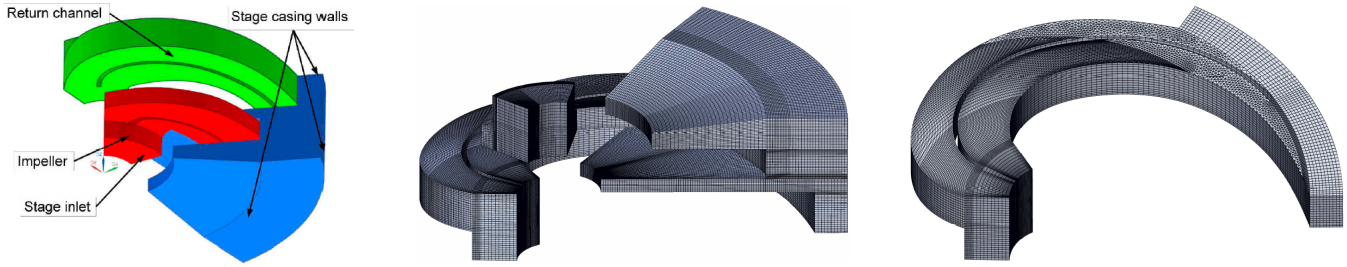

Figure 1. Computational domain and discretisation of the CFD approach suggested in [14]: (**a**) impeller (red), annular chamber (blue) and return channel (green) regions; (**b**) grid of the entire domain; and (**c**) view of the partially structured grid used for the return channel.

With regard to the discretisation practice, structured-, unstructured- and hybrid-type grids were adopted, with the grid type playing a major role on the predictions' accuracy. In fact, in a fixed numerical and physical modelling setup, the accuracy of the pump head prediction is in the order of 3.5% of the experimental datum, when structured grids are used, whereas it is roughly halved using unstructured grids. Focusing only on the more accurate models, it can be stated that approximately 1.5 million structured cells for stage are needed to obtain predictions dependent on the grid size by less than 1%, although Table 1 shows a strong spread in the values of cell numbers and cell size (not depend only on the reference publication year, i.e., on the available computation power).

From Table 1, it also clearly emerges the importance attributed by researchers to the interaction between adjacent stages: most of the references (12 out of 19) included all the stage counts in the simulated domain, and 3 [7,8,16] out of the 7 remaining included the first two stages. However, the accuracy achieved on the head and efficiency predictions by such large domain approaches is comparable with that achieved by the single-stage simulations performed by Roclawski and Hellmann [5], who concluded that the pre-rotation at the succeeding stages entrance, due to the residual tangential velocity component at the return channels exit, affects the stage performance but does not modify (appreciably) the stage efficiency and the velocity field at the impeller exit. In fact, the analyses performed by Wang et al. [10], who compared the turbulent kinetic energy distributions on the mean sections of the impellers and return channels belonging to four succeeding stages, showed a substantial flow similarity for all the stages succeeding the first one and indicated that the first stage's flow field differs from the flow field of the succeeding stages only in the innermost region of the impeller. An analogous conclusion was suggested by Li et al. [13], who stated that the head and absorbed power of the stages succeeding the first one are substantially equal to each other and lower than those of the first stage. On the other hand, the relatively limited accuracies achieved by calculations performed on all-stage domains, in which only one blade channel per stage was considered (see [15,21]), suggest the single-channel model approximation as more penalising than the single-stage one. This seems to be confirmed by the poor accuracies achieved by the calculations results presented in [3], which however also pay for the still limited development level of the CFD packages available at that time. In fact, the other single-stage single-channel calculations provided results for either some flow unsteadiness [4] or correction for the interaction between stages [14], and the obtained accuracy of the global performance prediction was not worse than that achieved by the other more complex and computationally expensive models summarised in the table.

Thus, it can be summarised that, as far as the stage global performance is concerned, the predictions from well-conceived, rather basic steady-state RANS calculations, exploiting the standard κ-ε turbulence closure on single-stage single-channel domains discretised with structured grids counting few hundred and thousand cell numbers, are not definitely worse than those achievable by more enhanced CFD approaches, being the simplifying

assumptions of the former counter-balanced by the computational cost constraints of the latter.

Research gap. In fact, a major issue is related to the inclusion in the CFD model of secondary geometrical features as impeller side gaps and sealings elements. Table 1 indicates that simulations performed using computational domains accounting for such features do not show a definite improvement in the accuracy achieved by calculations performed on similar domain and comparable grid type/size in which such secondary features were neglected. Among the many possible reasons for this failure of accuracy improvement, there is—in the case of sealing systems based on floating wear rings—a difficulty to know (also by experiments) the real axial position of the ring during the pump operation. In fact, [22] suggested a method to numerically model a sealing system with a floating wear ring but did not provide any experimental validation of the results obtained using the method. Regardless of the geometrical uncertainties, the inclusion of sealings and impeller side gaps in a CFD model strongly increases the computational cost of the simulation because the solution of the local flow field in such additional zones requires important grid refinements. The computational cost could be reduced exploiting some smart CFD-based simulation procedures as the one described by [23] and later by [24]. This procedure establishes how to perform the in-series simulation of different multistage pump sub-systems—disassembled from each other—and then use the data extracted from each sub-system's analysis to obtain the pump stage performance. It is worth mentioning that one of the key ideas to limit the computational effort needed to accurately solve the stage hydraulics relies on the disposal of the sealing elements' leakage flow characteristic (i.e., leakage flow rate vs. impeller head curve). According to the procedure, the latter should be obtained from 2D axy-simmetric CFD simulations of a domain made of: (i) a small annular region—extracted from the volume downstream of the impeller exit; (ii) the side gap at the impeller shroud; (iii) the sealing passage between (i) and (ii); (iv) the volume upstream of the impeller entrance; and (v) the sealing passage between (iv) and (ii). Unfortunately, this simulation approach does not solve the problem previously mentioned of knowing the exact geometric modifications to which some sealing systems are subjected in operation and, mostly, it neglects the effects of the tangential velocity at the impeller exit, therefore also losing its validity for all the several design solutions in which these effects play an important role in the secondary losses, as explained by [25]. This supports the statement that high-fidelity calculations are not able to definitely improve the prediction accuracy of the pump stage global performance achievable using some of the low-fidelity CFD approaches widely used in the past, mostly when the former experience uncertainties related to the fluid dynamics of the very same pump features neglected by the latter. Accordingly, when the results and effort of the experimental characterisation of a sealing system are useful for several designs sharing the same sealing solution, as for stock production multistage pumps, it could be convenient for manufacturers to perform a "once for all" characterisation of the sealing system, mostly if it would allow for less demanding and more accurate computations that are able to reduce the prototypes' testing activity in the development of a new multistage pump design.

Paper's specific aims. The paper proposes a new hybrid experimental-numerical method to simulate the multistage pumps' hydraulics. The method incorporates into a single-stage single-channel CFD approach the experimental characteristics of the pump's sealing system with the aim of obtaining a practical engineering tool suited to support the preliminary design of multistage pumps at the industrial level, where repeated simulations of several designs are necessary, and the best trade-off solution between accuracy and computational effort is of utmost importance. The aim of the paper is to present the entire method and validate its prediction capabilities on a real multistage compact-design pump.

Novelties and original contributions of the work. Differently from other CFD analysis methods proposed in the multistage pumps literature, in which either high-fidelity approaches were simplified to reduce their computational effort—at the cost of accuracy reduction—or experimental data were embedded in very detailed simulations—to further

increase their accuracy—, the originality of the method presented in this paper relies on its aim to improve the accuracy of simple calculations to increase the quality of the preliminary designs without increasing the time duration of the corresponding design phase, while shortening the duration of the succeeding optimisation phase. In addition to this, to apply the method, the sealing systems' characteristic of the pump under analysis was measured using a new test rig, designed to allow for testing a rather extended range of operations and design variants of the sealings. Finally, the validation of the hybrid experimental-numerical model extends behind the global hydraulic performance and includes the assessment of the pump stage axial thrust, whose experimental values were measured at different operating conditions using another original rig designed to test a single stage disassembled from the pump.

Structure of the paper. The key points of the multistage pump CFD modelling approach suggested in a previous authors' work are briefly summarised in the Background Literature Section, before presenting and explaining—in the following section—the concept of and the way to apply the hybrid experimental-numerical CFD method. The Material and Methods Section presents the multistage pump chosen as the benchmark for the hybrid method, the experimental characterisation of the sealing elements and the pump stage axial thrust measurements, required to apply the method and validate it, respectively. Finally, the predictions of the hybrid method are compared with the experimental data in the Results Section and the main findings are summarised in the Conclusions.

2. Background Literature

As mentioned in the Introduction, to improve the predictions of the single-channel calculations, without increasing the computational cost, the authors suggested in [14] a modelling approach, in which only the first stage of the multistage pump is considered, and the hydraulic performance of the succeeding stages is obtained by correction of the static head and the absorbed power predicted for the first stage, taking into account the pre-rotation existing at the succeeding impellers' entrance.

The suggested modelling approach extends the computational domain—as shown in Figure 1a for the case of a vertical multistage pump—from the single-channel of the impeller (the red-coloured region in the figure, which includes the short annulus upstream of the impeller eye), to a periodic azimuthal slice of the annular chamber at the impeller exit (blue-coloured region) and to one return channel, including the short annulus downstream of the vane exit (green-coloured region). Note that, if the return channels' blade counts differ from the impeller blade counts, a modification of the actual periodicity is required to limit the azimuthal width of the domain. Using the modelling approach, the domain just described shall be discretised with a fully structured grid for the impeller channel and the annular chamber, and a partially structured grid for the return channel. Figure 1b,c present the wireframe plots of the full-domain and return channel grids, respectively.

According to the numerical validation performed in [14], approximately 150 k cell numbers in the entire domain ensure differences from the asymptotic values of head and shaft torque (obtained by simulations on approximately 850 k cells) lower than 1% for steady-flow RANS computations ("frozen rotor" multi-reference-frame motion model) using the linear k-ε with standard wall functions ($25 < y+ < 70$) for the turbulence closure. However, when the cell numbers are increased to 530k, the difference from the asymptotic values of head and torque become almost negligible (less than 0.25%). Accordingly, it was decided to keep this grid density for all the calculations. With regard to the boundary conditions, fixed-flow rate and uniform static pressure are suggested at the domain entrance and exit, respectively.

The stages' interaction, responsible for the pre-rotation at the entrance of all impellers downstream of the first stage exit section, unloads the blades of the impellers following the first one and, consequently, reduces their power absorption (P_s) by the quantity ΔP_{ST}, defined as follows.

$$\Delta P_{ST} = \omega \, MF. \tag{1}$$

The two variables in the rhs of Equation (1) are the impeller angular velocity ω and the tangential momentum flux due to the pre-rotation at the impeller inlet (*MF*). The latter is equal to the tangential momentum flux at the first stage exit section. Thus, it can be easily calculated as a mass-weighted integral at the exit surface of the first-stage domain as solved by the CFD model.

The reduction in the stage hydraulic power can be obtained by the product of ΔP_{ST} for the first-stage efficiency η, assuming that such efficiency is not strongly affected by the pre-rotation at the impeller entrance. Finally, the decrease in the dimensionless static head for stage $\Delta\Psi_{ST}$, due to the pre-rotation, is attainable as follows.

$$\Delta\Psi_{ST} = \frac{\eta\ \Delta P_{ST}}{\rho\ q_v\ \omega^2 D^2}. \tag{2}$$

The not-already defined variables in the rhs of Equation (2) are the fluid mass density (ρ), the volume flow rate (q_v) and the pump impeller diameter (D). Since the first stage is not affected by pre-rotation, the total decreases in the power and head coefficient of the multistage pump are n−1 times the corresponding decreases calculated using Equations (1) and (2), respectively, where n is the stage counts.

The model just summarised will be hereafter referred to as "pure" CFD model, in order to clearly distinguish it from its evolution, which is the subject of this paper. For the sake of the reliability assessment of the pure CFD model, Figure 2a,b compare the measured stage static head (H_{ST}) and efficiency curves (continuous lines) with the CFD predictions (orange markers) for the six-stage vertical pump (the subject of Section 4.1) used as the benchmark in this work. Figure 2a also includes the static head values as predicted by CFD without correction for the pre-rotation at the impeller entrance (blue markers), to demonstrate its role in the prediction capabilities achieved by the pure CFD calculations. In accordance with the assumption that pre-rotation does not affect the stage efficiency, the latter is not included in Figure 2b, being perfectly superimposed to the pure CFD prediction.

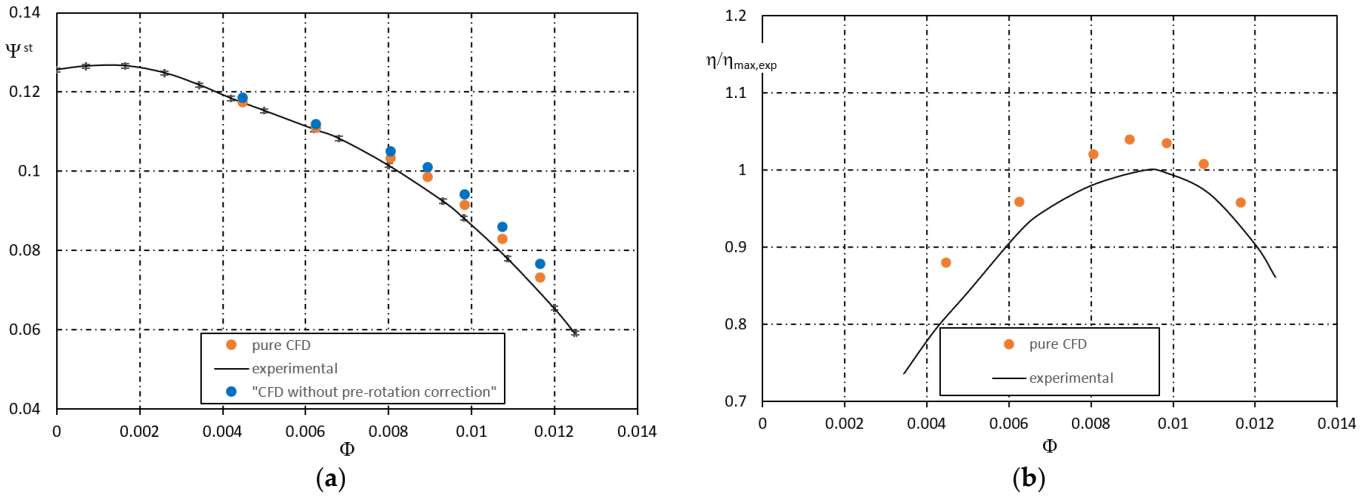

Figure 2. Comparison of the stage hydraulic performance for a six-stage vertical pump as measured (continuous line) and predicted by pure CFD (orange markers) and CFD without pre-rotation correction: (**a**) head coefficient vs. flow rate coefficient; and (**b**) efficiency to experimental maximum efficiency ratio vs. flow rate coefficient.

All the CFD simulations discussed in this paper were implemented into the OpenFoam 2.1.1 environment.

The dimensionless parameters used hereinafter to present the performance data are the head coefficient, flow rate coefficient and absorbed power coefficient, whose definitions are in accordance with Equation (3).

$$\Psi^{ST} = \frac{gH_{ST}}{\omega^2 D^2} \qquad \Phi = \frac{q_v}{\omega\, D^3} \qquad \Pi = \frac{P_s}{\rho\, \omega^3 D^5} \tag{3}$$

As stated in the Introduction with reference to the data collected in Table 1, the head and the absorbed power predicted using this CFD approach match the experimental data with a level of confidence comparable to that of more computationally demanding models.

3. Hybrid Experimental-Numerical CFD Method

The hybrid experimental-numerical CFD method upgrades the pure CFD modelling approach. It was conceived to account for the effective volumetric losses due to leakages without the need of simulating them by CFD, owing to the availability of experimental data. In the following, the concept, expected outcomes, hints and approximations of the method are presented item by item.

Concept of the method. The stage pressure field as obtained from the pure CFD can be used to estimate the pressure differences across the sealing systems of the impeller and the return channels. These pressure differences, in turn, permit the derivation of the impeller and return channel leakage flow rates from the characteristic curves obtained from the experimental test of the impeller and return channel sealings. Since the pressure field available from the pure CFD does not account for the effect of the leakage flows—which alter the pressure field to reduce the leakages themselves [25]—to obtain an accurate estimation of the stage hydraulics, it is necessary to iterate the CFD calculations until predicted leakages converge to the values actually imposed as boundary conditions.

The procedure must be conducted for all the operating conditions chosen to define the pump performance curves. However, if the calculation is aimed at only estimating the global hydraulic performance of the stage, the approximated determination of the impeller leakage, as obtained from the use of the pure CFD pressure field, allows to improve the stage static head and efficiency curves that are already available (from the pure CFD) by the correction of the stage flow rate values via the subtraction of the impeller leakage. Such post-process hybridisation is hereafter referred to as "simplified hybrid method" to distinguish it from the complete method.

Outcomes of the method. The main outcome is the improvement of the stage hydraulics prediction. This improvement also permits the improvement of the estimation of the axial thrust. The latter can be derived by the summation of the force components along the shaft axis resulting from the surface pressure integrals on each wetted surface of the impeller.

Hints for the practical application of the method. As previously stated, to determine the leakage flow rates across the sealing systems the leakage sections must be precisely defined in the CFD model. With reference to Figure 3, the pressure difference across the impeller sealing system can be approximated as the difference between the area-weighted integrals of the static pressure on the "leakage 1" surface and the total pressure on the "inlet" surface, whereas the pressure difference across the return channel sealing system can be approximated as the difference between the static pressure integrals on the "outlet" and "leakage 2" surfaces. The estimated leakages shall be applied as the mass flow boundary conditions at the "leakage 1" (outlet condition) and "leakage 2" (inlet condition) surfaces. The complete set of boundary conditions required to apply the method are summarised in Table 2.

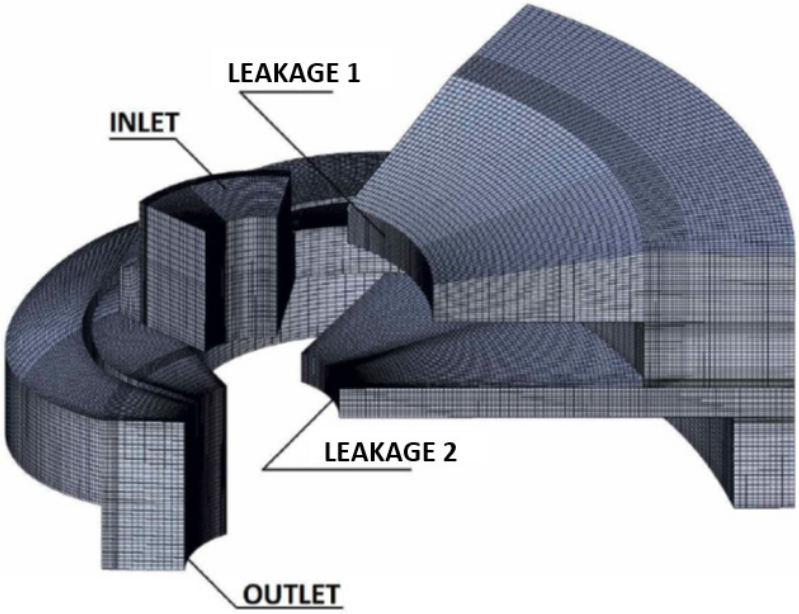

Figure 3. View of the grid used for the stage simulation with the indication of the sections across which the leakages are assumed to occur according to the hybrid method.

Table 2. Boundary conditions to be imposed in accordance with the hybrid experimental-numerical method.

Region	**Regions** *		
Surfaces	**Impeller**	**Annular Chamber**	**Return Channel**
Entrance	Mass flow inlet (I)	Sliding interface	Internal interface
Exit	Sliding interface	Internal interface	Pressure outlet (I)
Leakage 1 †	-	Pressure outlet	-
Blade	No slip wall	-	No slip wall
Leakage 2 †		Mass flow inlet (II)	-
Side walls	No slip wall	No slip wall	No slip wall
Azimuthal surfaces	periodic	periodic	periodic

* see Figure 1a. † see Figure 3.

From a theoretical point of view, the hybrid numerical–experimental method can be applied in a twofold way:

(a) By fixing the target flow rate, i.e., the stage flow rate, and summing to it the calculated impeller leakage to obtain the impeller flow rate. This way is more convenient for model validation purposes or, more generally, when CFD results shall be compared to some available experimental data.

(b) By fixing the domain inlet flow rate, i.e., the impeller flow rate, and subtracting from it the calculated impeller leakage to obtain the stage flow rate. This way is easier to apply because it does not require the update of the inlet boundary condition moving across the succeeding solutions and this strongly favours the convergence (the main hydraulics of the pump stage remain almost unchanged, since the major differences between succeeding solutions occur in the impeller side gaps).

Approximations of the method. In addition to the assumption of the negligible free static pressure recovery of the residual swirl at the return channel exit, implicit in the way just suggested to estimate the pressure difference across the corresponding sealing system, it is worth noting that, in the real stage, the useful flow rate from the return channels equals the stage flow rate, because the leakage at the exit of the return channels crosses the volume between the impeller and the return channel disks and re-enters the return channels. In contrast, in the hybrid experimental-numerical CFD model, the return

channels' leakage enters the domain from the "leakage 2" surface and outflows from the domain exit section instead of the clearance. Rigorously, this means that the flow rate across the annulus downstream of the return channels exit, as predicted by the hybrid CFD method, exceeds the effective flow rate at the stage exit. However, from a practical point of view, such excess of flow rate does not affect the accuracy of the return channels' hydraulic performance predictions.

Finally, the computational time required to calculate one operation point on the domain counting approximately 530 k cell numbers is approximately 3 h on a dual processor computer (Intel Xeon CPU E5-2687W 0 3.10 GHz—16 cores and 32 threads).

4. Materials and Methods

In addition to the geometrical data of the multistage pump, the hybrid numerical–experimental method requires for its application the availability of experimental data on the hydraulic behaviour of the sealing elements. Moreover, the availability of axial thrust data permits the widening of the validation of the simulation approach far beyond what was allowed by the comparison between the predicted and measured hydraulic performance curves. Accordingly, two experimental campaigns were undertaken to measure the hydraulic behaviour of the sealing elements used in the benchmark pump and the axial thrust acting on the pump shaft. This section presents the benchmark pump in the first subsection and focuses on the just-introduced two experimental campaigns in the second and third subsection.

4.1. Benchmark Pump

The machine under analysis is a vertical 6-stage pump with in-line suction and delivery, manufactured from cold-formed stainless-steel sheets, already studied in [14]. Figure 4a shows a section drawing of the pump. The 6 stages are identical and incorporate a six-blade radial-flow impeller (ID 50.00 in the figure) surrounded by a cylindrical chamber with a diameter (D_{ST}) in the order of 100mm, which collects the flow and feeds six radial-flow return channels. A floating wear ring (ID 40.02 in the figure) acts on the neck of each impeller to keep the volumetric efficiency to a satisfactory level through the reduction in the backflow from the gap outside the shroud disk towards the impeller suction. The other backflow due to the leakage of the return channels is controlled by the clearance between the hole in the return channel disk and the surface of the pump shaft (ID 30.00). Figure 4b sketches the meridional section of an intermediate stage and shows its main geometrical parameters. The white and red arrows in the figure indicate the main and leakages flow paths, respectively. Details of the stage geometry are reported in [26].

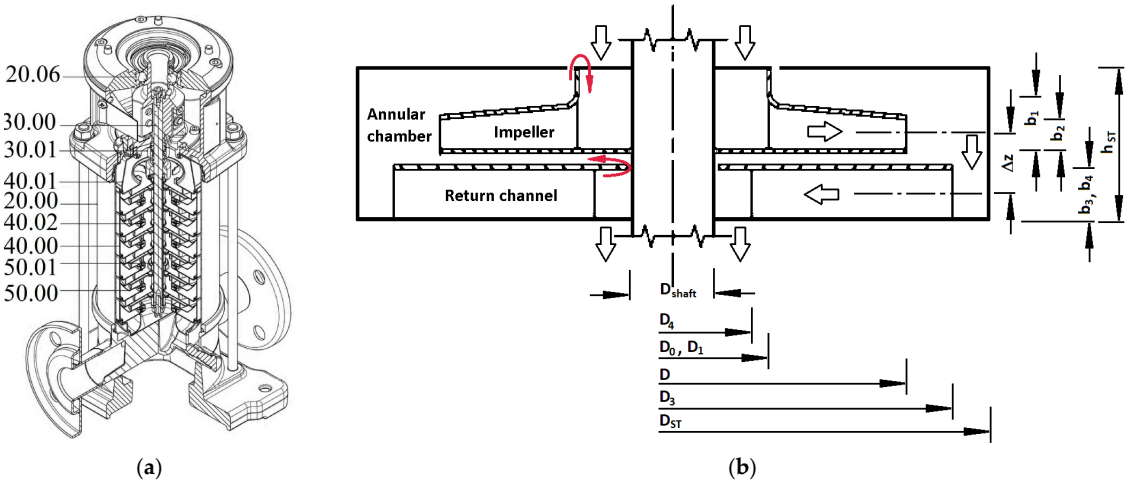

(**a**) (**b**)

Figure 4. Benchmark pump: (**a**) axonometric view of the machine; and (**b**) meridional section of an intermediate stage. Adapted from [14].

4.2. Sealing Elements' Characterisation

A series of experimental tests was performed to measure the impeller and return channel leakage flows. From the pump hydraulics' point of view, the flow rate recirculation in the return channels is not as critical as the impeller recirculation for the head and efficiency performance of common designs [25]. Accordingly, the major experimental effort was devoted to the performance of the impeller's wear ring sealing system, which was measured as a function of the sealings' design, installation, and operating conditions. In contrast, only one design was considered for the return channels' leakage tests.

The description of the test rig conceived for the leakage tests, the testing protocol and the test results are the subject of the next three sub-subsections.

4.2.1. Leakage Flow Test Rig

The core of the test rig is the test chamber, whose internal volume shape copies the inner volume of the real pump stage to make possible the mounting of different sealing systems on the intermediate wall dividing the high-pressure region from the low-pressure one. The chamber casing is modular and allows for the incorporation of inserts with different shapes of their wetted surfaces, to permit the simulation of either the impeller wear ring sealing or the leakage across the clearance between the pump shaft and return channels. Figure 5a shows a section drawing of the test chamber configured for the impeller wear ring leakage test. The figure also shows the position of the pressure taps drilled in the chamber casing to measure the static pressure in the high- and low-pressure environments and close to the leaking section. A strain gauge transducer with 5 bar pressure range and 0.2% accuracy (based on the full-scale reading) is connected to each pressure tap. The casing of the test chamber is connected to the pump electric motor, whose shaft enters the chamber to permit: (i) mounting of dummy impellers (metal disks machined to simulate the impeller bulk and its external geometry)—in the case of wear ring sealing tests; and (ii) simulating the shaft return channels' clearance—in the case of return channel leakage tests.

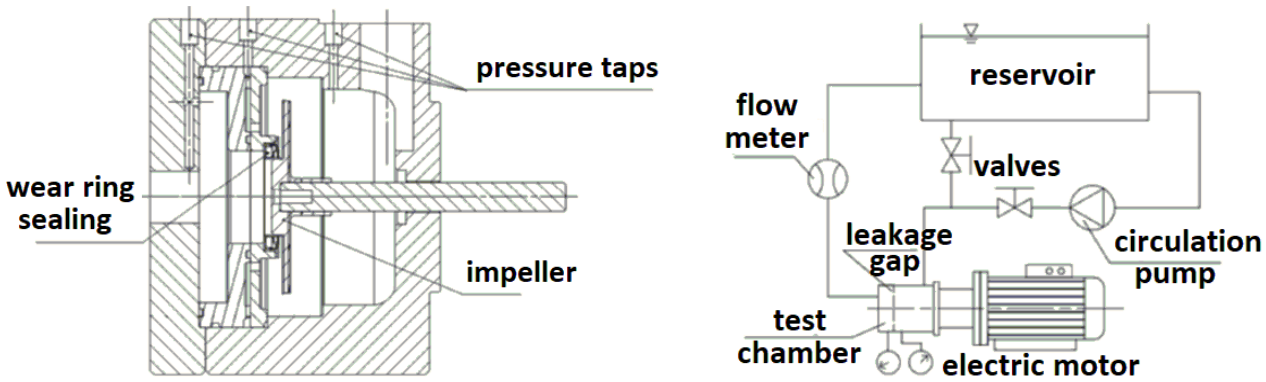

Figure 5. Experimental setup for the leakage flow tests: (**a**) test chamber configured for the wear ring impeller sealing test; and (**b**) scheme of the leakage flow test rig.

The test chamber is embedded on the test rig in accordance with the scheme in Figure 5b. The rig is fed by a reservoir open to the atmosphere, from which a circulation pump sucks the water to be delivered to the high-pressure inlet of the test chamber. A valve system upstream of the test chamber permits the setting of the high-pressure level to the desired value. The low-pressure exit of the chamber discharges the water in the return pipe to the reservoir. This return pipe is equipped with a flow rate sensor (with full scale and accuracy equal to 15 m^3/h and 0.2% of the reading datum, respectively), allowing for the measurement of the leakage flow.

4.2.2. Testing Protocol

The characterisation of the impeller and return channel leakage flow for a specific design requires the measurement of the leakage flow rate at several values of the pressure difference existing between the high- and low-pressure environments connected by the leakage flow path. To this end, the shaft rotational speed is fixed to the desired value—by means of the inverter power electronics—and the flow control valves system is regulated to obtain the desired leakage, measured by the flow meter. When the stable operation of the test rig is achieved, the leakage and corresponding pressure difference data pair of the specific operating condition are obtained by time averaging the signals recorded from the three pressure sensors and flow meter (all acquired at a frequency equal to 50 Hz for a 10 s time window). Once the data of the specific operating condition are stored, the flow control valves system is set to obtain a different operating condition and the data acquisition restarts. Starting from the zero-leakage operation, the procedure is repeated at progressively increasing flow rates until the maximum high-pressure value achieved upstream of the leakage path at the nominal operating condition is achieved.

It is worth noting that, at a zero leakage flow rate and zero rotational speed, zero difference in pressure was measured from the taps mounted upstream and downstream of the wear ring sealing in the test rig, respectively, whereas this was not the case at the nominal rotational speed. This is consistent with the difference in the radial position of the two pressure taps, which are not subjected to the centrifugal effect only when there is no rotation. Accordingly, the pressure difference data acquired at the nominal speed of the impeller shaft were corrected by subtraction of the pressure difference measured when the shaft was at rest.

For the impeller wear ring, the investigated characteristics ascribable to the sealings' design were: the configuration of the ring seat (closed cage, semi-open cage and no cage), the nominal dimensionless diameter of the ring (equal to 42% or 50% of the impeller diameter D) and the ring stiffness (modified by using rings made of PPS, 2.6 GPa Young modulus, or PTFE, 0.4 GPa Young modulus). Three axial positions of the impeller were considered to account for the sealings' installation issues: the nominal position, in which the total height of the wear ring superimposes to the annular surface generated from the impeller shroud disk; and other two positions, in which the impeller is shifted towards the return channel wall by 15% and 33% of the wear ring height. Finally, the wear ring was tested with the impeller shroud disk both at rest and at the nominal rotational speed to cope with the sealings' operating conditions. Table 3 summarises the characteristics of the sealing system investigated in the 9 impeller sealing tests, which are identified hereafter by their specific test ID.

Table 3. Characteristics of the wear ring sealing investigated in each experimental test.

Test ID	**Cage Design**			**Ring Size d_{WR}/D [-]**		**Ring Flexibility E [GPa]**		**Ring—Impeller Shroud Disk Spacing sp/h_{WR} [-]**			**Shaft Speed N [rpm]**	
	Open	**Semi**	**Closed**	**0.42**	**0.5**	**2.6**	**0.4**	**0 (nom)**	**0.15**	**0.33**	**0**	**2900**
I			X	X		X		X				X
II	X			X		X		X				X
III			X	X			X	X				X
IV		X		X			X	X				X
V	X			X			X	X				X
VI			X		X	X		X				X
VII			X	X		X			X			X
VIII			X	X		X				X		X
IX			X	X		X			X		X	

The leakage across the shaft return channels clearance was measured only for a shaft-to-hole diameter ratio (D_{shaft}/d_{HRC}) approximately equal 0.92 (a value reasonable for the combination of the application and manufacturing technology under analysis).

4.2.3. Sealing Performance Data

In this section, the main results of a thorough experimental campaign dedicated to the characterisation of the sealing systems appropriate for vertical pumps manufactured by the steel metal- sheet-forming technique, and performed in the framework of the activity documented in [27], which deals with the hydraulic design of multistage compact-design pumps, are briefly summarised. In particular, the characteristics of the impeller wear ring and the return channels sealings are reported as performance graphs in the following. Since the detailed discussion of these results is out of the scope of this paper, the reader is referred to [27] for further information.

Figure 6 reports the leakage flow rate (q_L) measured for all the test conditions listed in Table 3 as a function of the pressure difference (Δp). The shaded area indicates the range of performance covered by the experiments.

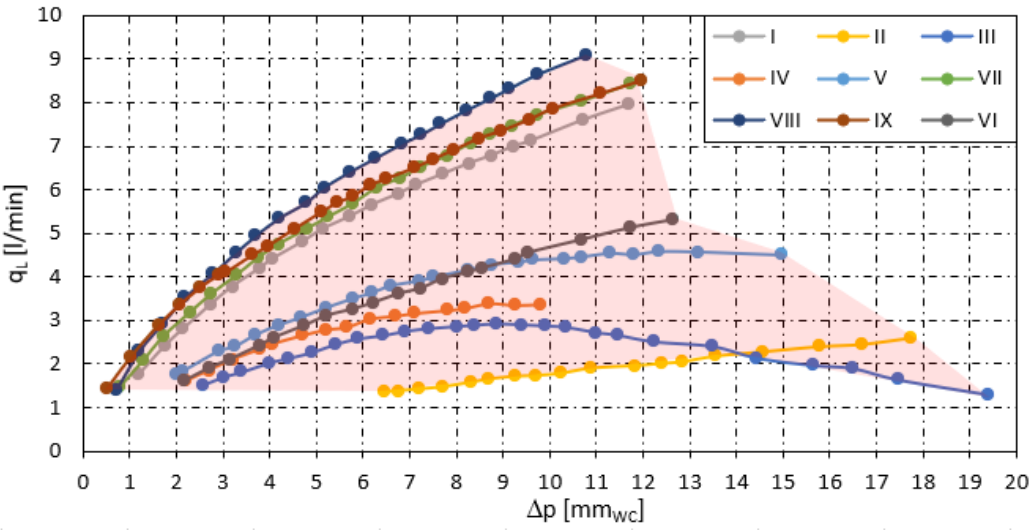

Figure 6. Effect of the wear ring features on the impeller leakage as a function of the pressure difference (measured in the water column, mm) across the sealing. See Table 3 for the ring features specific to each test ID reported in the figure legend.

In contrast, each frame in Figure 7 presents only the test conditions relevant to the analysis of a specific sealing feature among those considered and compares them to the entire sealing operation range investigated, to immediately quantify the importance of the specific feature on the sealing performance. In particular, Figure 7a–d demonstrate the major role of the wear ring's site design, stiffness, and size, in the control of the impeller leakage.

The results obtained from the return channel leakage test are presented in Figure 8, in which the same performance parameters and graphical convention as Figures 6 and 7 were adopted. The comparison of the leakage flow rate data (orange markers) with the operating range measured for the several wear ring sealing solutions (shaded area taken from Figure 6), in the first instance, could suggest the need for an increase in D_{shaft}/d_{HRC} to reduce the return channels leakage, which is noticeably higher than the impeller wear ring leakage at an equal pressure difference. This is not the case, because the high-reaction design of centrifugal pump impellers leads to values of pressure differences between the delivery and suction of the impeller by far higher than those arising between the exit and entrance of the return channels.

Interestingly, the dotted curve used to approximate the return channel leakage data was obtained from the theoretical orifice flow model using the real geometrical area as the flow passage section and the unit value as the discharge flow coefficient. The very good approximation of the experimental data justifies the reduced effort devoted in the return channel leakage tests. In fact, the performance attainable from the geometries with different values of D_{shaft}/d_{HRC} can be very well predicted by the analytical model.

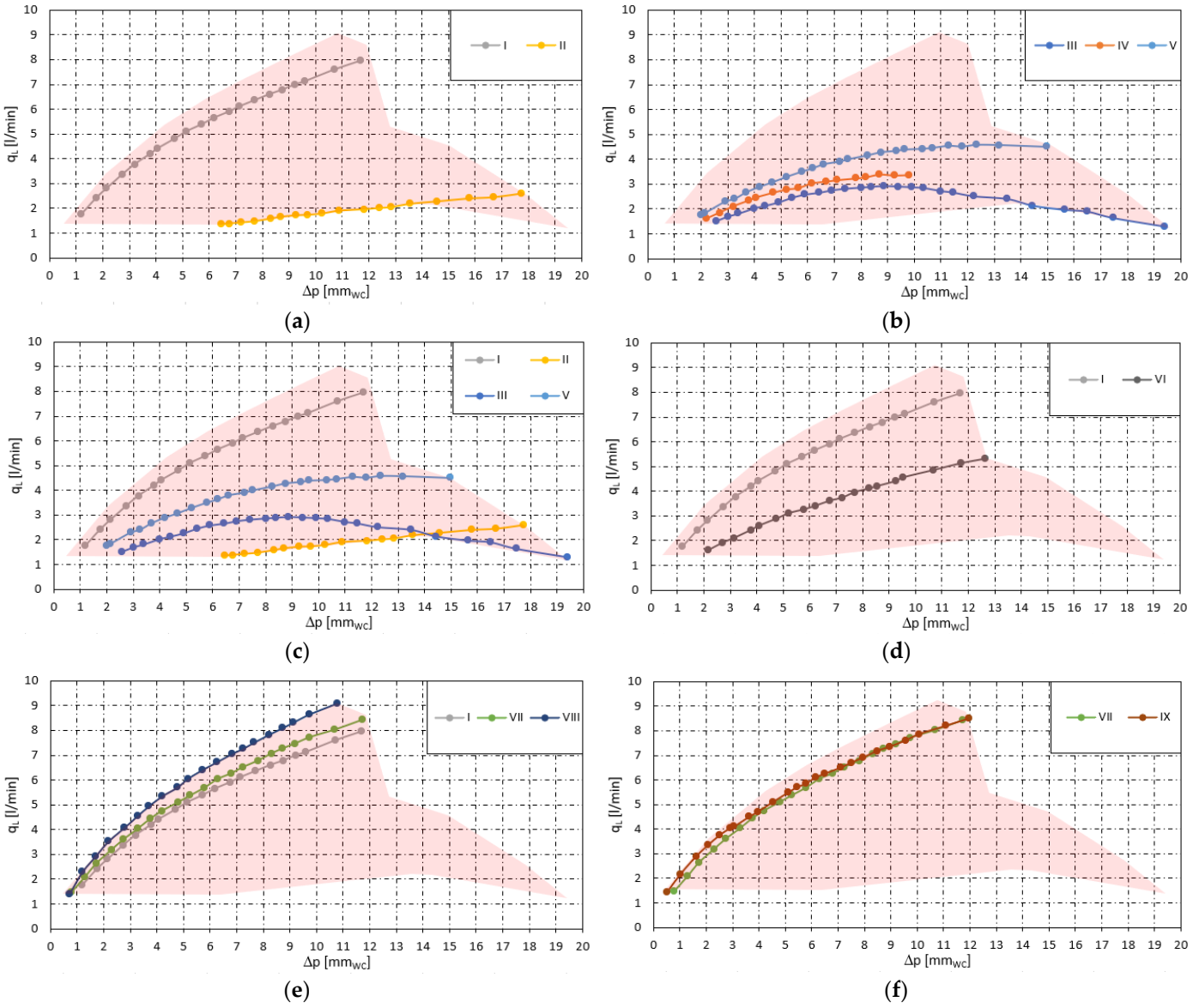

Figure 7. Performance of the wear ring impeller sealing as a function of the design, installation, and operating condition features of the sealing: (**a**) closed vs. open cage, i.e., I vs. II, for the flexible ring (PTFE); (**b**) closed vs. semi-open vs. open cage, i.e., III vs. IV vs. V, for the stiff ring (PPS); (**c**) closed vs. open cage for flexible (PTFE) and stiff (PPS) rings, i.e., I vs. II and III vs. V, respectively; (**d**) smaller vs. larger size ring, i.e., I vs. VI, for flexible rings (PTFE); (**e**) nominal vs. medium vs. large ring-impeller shroud spacing, i.e., I vs. VII vs. VIII, for flexible rings (PTFE); and (**f**) zero vs. nominal rotational speed of the impeller shroud disk, i.e., VII vs. IX.

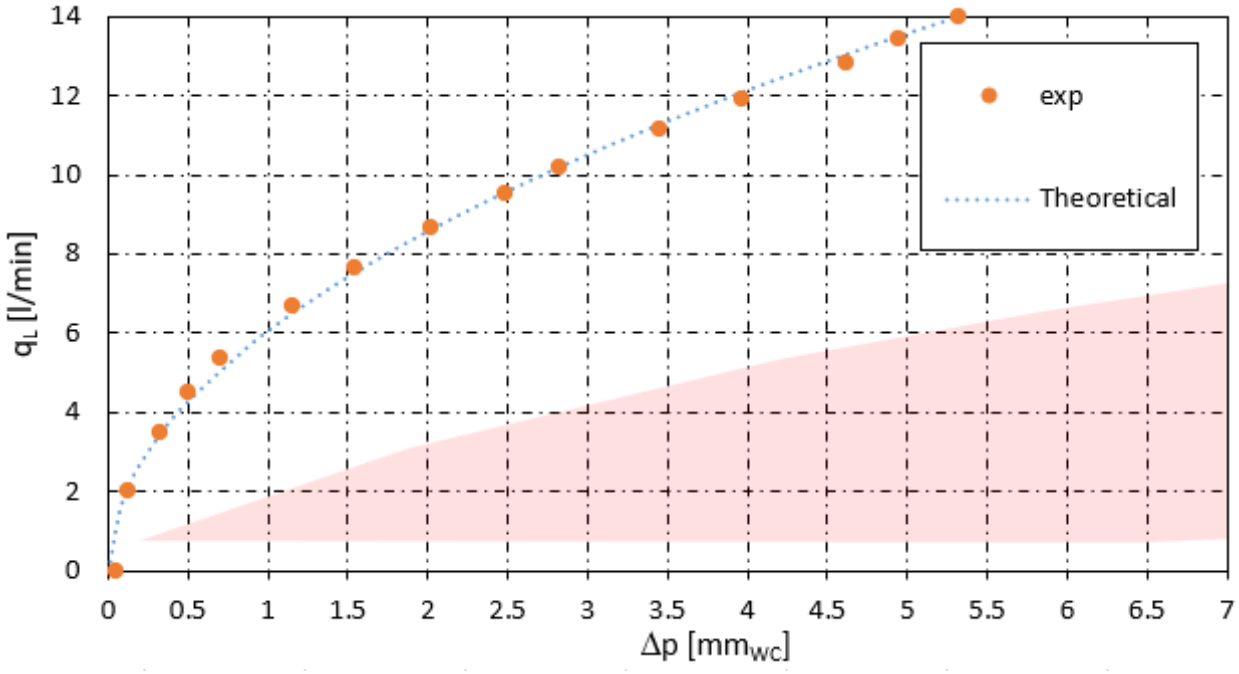

Figure 8. Return channel leakage flow for 0.92 pump shaft to hole ratio (markers) compared with the theoretical orifice model (dotted line) and the operation range of the wear ring sealings tested in this work (shaded area).

4.3. Axial Thrust Measurement

Force measurements were performed for most of the stage operating range at the nominal rotational speed of the impeller.

The descriptions of the test rig conceived for the axial thrust's measurements, the testing protocol and the test results are the subject of the next three sub-subsections.

4.3.1. Experimental Apparatus

Figure 9 shows the conceptual sketch of the apparatus developed for the axial thrust's measurements. It is composed by:

- A first shaft (1), directly coupled to the pump shaft at one end and to a fixed transversal beam (2) by means of ball bearings (3) at the other end. The bearings are pushed against the shaft shoulder by the upper flange, which preloads them to avoid both the internal gap and the axial motion of the shaft relative to the transversal beam.
- Strain gauge dynamometers (5), interposed between the transversal beam (2) and the fixed frame. The dynamometers are fixed to the beam (2) by means of spherical joints (plugs and swivel eyes) to minimise the parasitic loads due to the bending moment induced on the beam by any axial load exerted on the shaft.
- A second shaft (4) interposed between the electric motor shaft, to which is directly flanged, and the first shaft, to which it transfers through a sliding joint only the mechanical torque (required by the pump operation).

This apparatus is therefore suited to measure the axial thrust (dynamometers signal) and transfer it to the frame without loading the motor shaft. Because of the internal friction, parasitic loads and misalignments during operation, an accuracy equal to ±5% of the axial thrust datum was estimated based on the tests' repeatability.

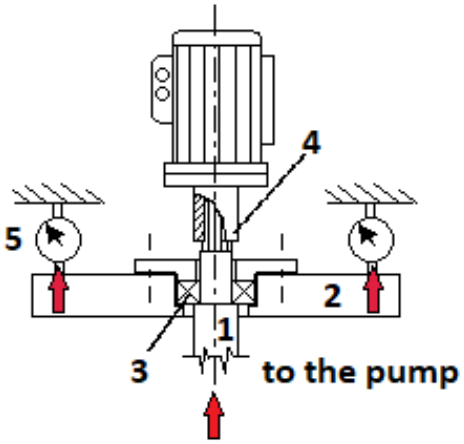

Figure 9. Conceptual sketch of the experimental apparatus for the axial thrust measurement. The main components are: first transmission shaft (1)—to the pump; transversal beam (2); ball bearings pair (3); second transmission shaft (4)—to the motor; and dynamometers (5). The arrows indicate the path of the load exerted by the axial thrust.

4.3.2. Testing Protocol

The axial thrust's measurements were acquired during hydraulic performance tests of the six-stage vertical pump, performed in an ISO 9906-compliant test rig at a constant rotational speed. The tests were performed after having removed the ball bearing placed at the motor flange of the pump and having interposed the apparatus described in the previous sub-subsection between the electric motor's shaft and the pump's shaft to support the entire load due to the axial thrust. The signals from each dynamometer were acquired at the same frequency and for the same time duration as for the leakage tests and summed each other. The final value of the axial thrust per stage at a specific operating condition was obtained by dividing the mathematical averaging of the raw data by the stage counts. The acquisition was repeated for all the operating conditions chosen for the pump hydraulic performance test.

4.3.3. Axial Thrust Data

Figure 10 shows the dimensionless axial thrust AT_S defined in accordance with Equation (4), in which T is the axial thrust per stage.

$$AT_S = \frac{T}{\rho\,\omega^2\,D^4} \tag{4}$$

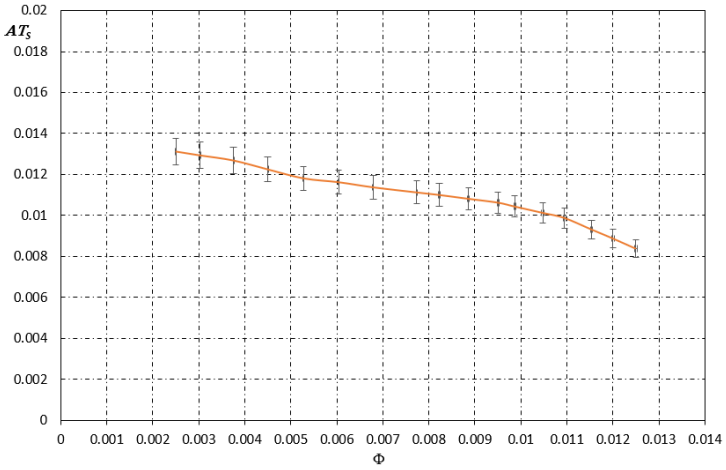

Figure 10. Dimensionless stage axial thrust as a function of the pump flow rate coefficient. Vertical and horizontal error bars indicate the uncertainties due to the force and flow rate data accuracy.

As expected for most of the vertical multistage pump designs, the axial thrust noticeably decreases as the pump flow rate increases, so that the qualitative AT_S trend resembles the corresponding trend of Ψ. Accordingly, the most relevant data from a design point of view are those measured at flow rates lower than the design duty.

5. Results

Figure 11a compares the stage pressure coefficient and absorbed power coefficient as a function of the flow rate coefficient as obtained for the benchmark pump from the ISO 9906 experimental tests (continuous lines) and the hybrid numerical–experimental CFD model (green markers), built in accordance with the guidelines reported in Section 3. Note that the sealing elements' experimental data included in the hybrid model were those previously indicated as test ID I, for the impeller wear ring, and those reported in Figure 8, for the return channel sealings.

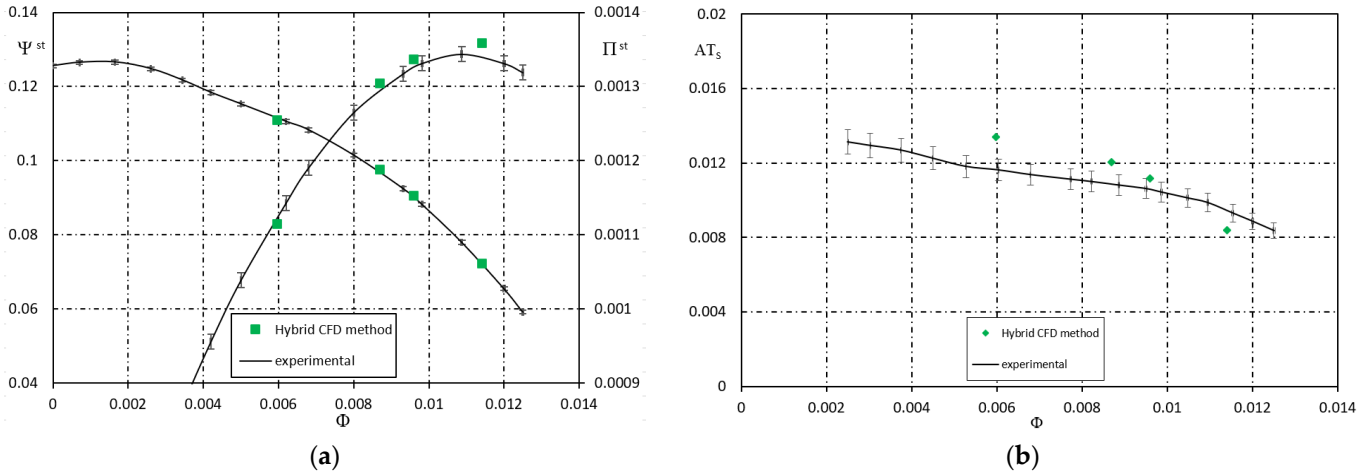

Figure 11. Comparison between the experimental data (continuous lines) and predictions from the hybrid numerical–experimental (green markers) models for an intermediate stage of the benchmark pump: (**a**) hydraulic performance (pressure coefficient—left ordinate; and absorbed power coefficient—right ordinate); and (**b**) axial thrust coefficient.

The method can perfectly match the head curve measured for the stage of the benchmark pump in the entire operating range of the machine.

Figure 11b superimposes the measured axial thrust coefficient (continuous line fitting the average measurements data, indicated by markers centred in the middle of the error bars) to the CFD predictions (green markers) derived, as explained in Section 3, by summation of the axial component of the force vectors acting on the impeller wetted surfaces. The hybrid numerical–experimental model predicts the axial thrust with an average accuracy approximately equal to 5%. In particular, in the four operating conditions simulated with the model, the relative difference between predictions and experimental data never exceeded 14% (12%, +9.5%, +5.9% and −14%, moving from lower to higher flow rates).

It is interesting to compare these results against those obtained by the CFD model proposed by Zhou et al. in [7], which is the one, among those summarised in Table 1, scoring the best accuracy in the prediction of the global performance at the best efficiency point, and which was in [28] supplemented by experimental measurements of the axial thrust. At the best efficiency point, the hybrid method allows the achievement of a better accuracy than the model by Zhou et al. [7] in the prediction of the static head (approximately 0.7% against 3%) and efficiency (approximately 0.2% against 1%), and a worse accuracy than the model by Zhou et al. [28] in the prediction of the axial thrust (approximately 12% against less than 5%).

Discussion

Figure 12a,b compare the predictions of the hybrid method to those obtained using the pure CFD approach summarised in the Background Literature Section. The improvement in the global performance prediction obtained with the hybrid method is rather clearly appreciable from Figure 12a. In particular, the differences in the static head and absorbed power predictions are limited, but appreciable, at higher and lower Φ values. On the other hand, the improvement in the stage axial thrust is definitely evident. In fact, looking at Figure 12b, although the overall trend of the axial thrust vs. Φ curve as predicted by the pure CFD method is rather good (and perhaps in better agreement with the experimental data trend reported in Figure 11b than that predicted by the hybrid method), the underestimation of the axial thrust values, if compared to those predicted by the hybrid method, exceeds the factor of 2.5 in the entire stage operating range, with the average relative deviation from the experiments of the hybrid method prediction being limited to approximately 5%, as already shown in Figure 11b. Such a noticeably different behaviour of the two models is explained by the influence of the leakage flows on the axial thrust, which is markedly stronger than the corresponding influence on the hydraulic performance.

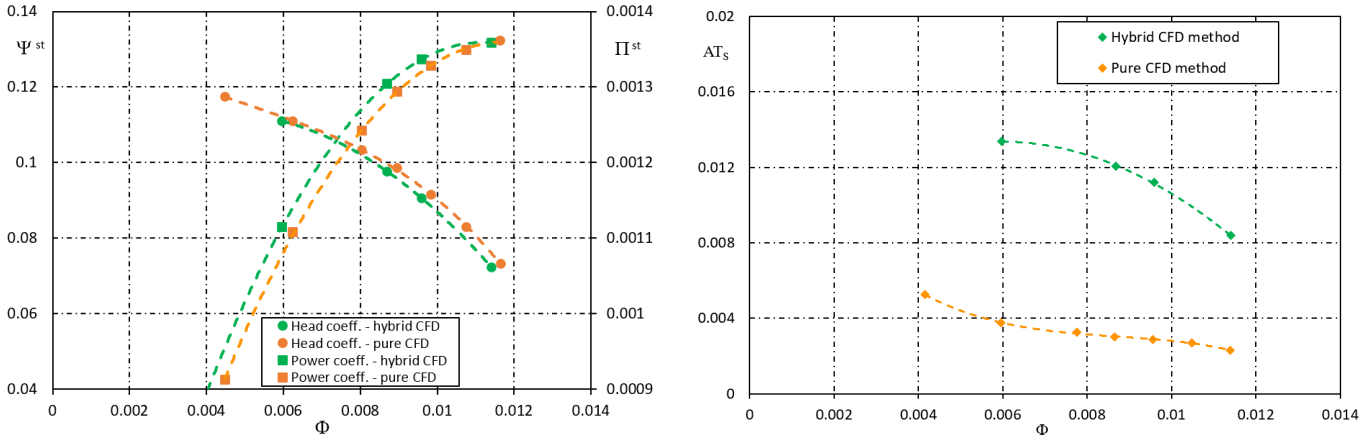

Figure 12. Comparison between CFD predictions obtained using the pure CFD (orange markers) and hybrid (green markers) methods for an intermediate stage of the benchmark pump: (**a**) hydraulic performance (pressure coefficient, left ordinate; absorbed power coefficient, right ordinate); and (**b**) axial thrust coefficient.

According to [25], the neat thrust acting on the impeller depends mainly on small differences in the pressure distribution on shroud and hub disk external surfaces facing the impeller side gaps. In fact, Figure 13a,b show the pressure contours and velocity vectors on a meridional section of the fluid domain outside the impeller and return channels, as predicted by the pure CFD and hybrid numerical–experimental model, respectively. It is apparent from the comparison of the two flow fields, how the return channels leakage, moving radially outwards, and the impeller leakage, moving radially inwards, modify the pressure field in the side gaps region (i.e., the region responsible for the axial thrust) without imposing a noticeable modification to the pressure in the outermost region (i.e., the region responsible for the pump head).

Most interestingly, these results suggest the following design indication: the reduction in the leakage flow rates attainable by an improvement in the sealings characteristics, although very slightly appreciable in terms of hydraulic performance, may offer substantial benefits in terms of axial thrust reduction.

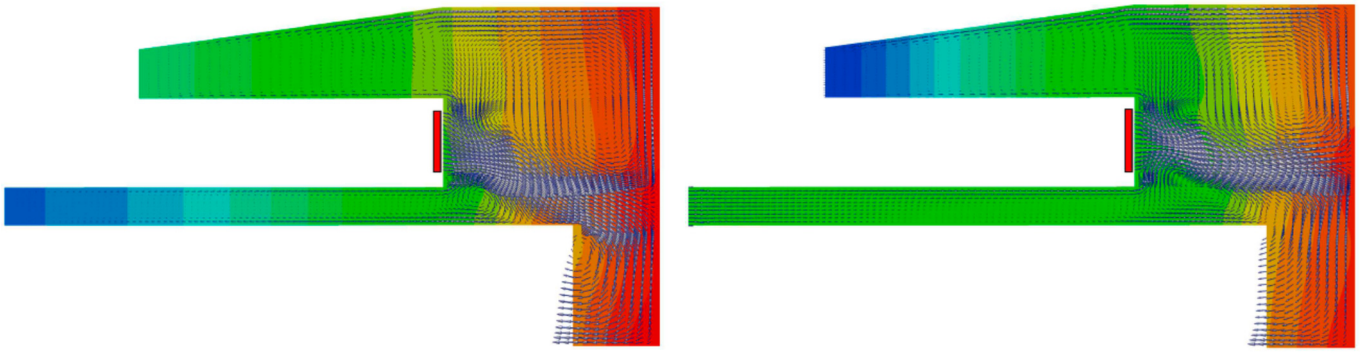

(**a**) (**b**)

Figure 13. Pressure field and velocity vectors in a meridional plane of the stage casing (the red strip indicates the impeller exit) as predicted by: (**a**) pure CFD approach; and (**b**) hybrid model with the inclusion of the impeller and return channels' leakages.

Finally, these results help to explain the lower accuracy in the prediction of the axial thrust shown by the hybrid method against the results of the CFD model reported in [28]. In fact, the comparison of the geometrical domain used here to study the benchmark pump and that used in [28] suggests that the lower level of feature simplification (see the average cell size in Table 1) and the lower relative size of the impeller side gaps (which likely affects the fidelity of the local flow field estimated by the CFD) characterising the model in [28] are two reasons for the better accuracy of the latter in the prediction of the axial thrust.

6. Conclusions

A hybrid numerical–experimental method to predict the hydraulic performance and the mechanical loads of multistage pumps was presented together with the guidelines necessary for its application to any multistage pump design. The method upgrades a CFD approach suggested in a previous work, which is based on single-channel single-stage computations corrected to account for the interaction between succeeding stages. The peculiarity of the hybrid numerical–experimental method presented in this paper relies on the incorporation of wear ring and return channels' leakage flows data obtained from experiments, which avoid the complicated task of simulating them by CFD. The method was validated against the experimental data collected from a stock production six-stage vertical pump. In particular, the results obtained using as leakage flow data the measurements performed on an "ad hoc" designed test rig demonstrated that the suggested hybrid numerical–experimental method:

- Is able to further improve the hydraulic performance predictions achievable using pure CFD calculations in accordance with a simplified approach, which, however, allows for an accuracy comparable with that of the more demanding computational approaches suggested in the literature.
- Permits a prediction of the head curve that fits very well the experimental data and an accuracy in the prediction of the absorbed power curve not worser than 1.5% in the entire operating range of the considered pump stage.
- Allows for a reliable estimate of the mechanical loads on the structural components of the pump, as demonstrated by the difference obtained between the axal thrust predictions and the corresponding data measured using an original test rig, which never exceeded 14% in the considered operating range of the pump. This accuracy cannot be achieved by other CFD approaches requiring comparable computational efforts.

According to these findings, the hybrid method presented in this paper reveals to be a very useful tool to support the design of stock-production multistage vertical pumps for which the manufacturer usually already disposes of the leakage flow characteristics from existing comparable designs. In particular, the use of the pure CFD approach accounting only for the stage interactions—to assess the hydraulic performance of a new design—

followed by the use of the hybrid numerical–experimental method to assess the mechanical feasibility of the most promising design is suggested as an effective package to aid a design process suited to time and cost deemed as industrially acceptable.

Author Contributions: Conceptualization, F.F. and M.M.; methodology, F.F. and M.M.; software, F.F.; validation, F.F.; formal analysis, F.F.; investigation, F.F.; resources, F.F.; data curation, F.F. and M.M.; writing—original draft preparation, M.M.; writing—review and editing, M.M.; visualization, M.M. and F.F.; supervision, M.M.; project administration, M.M.; funding acquisition, F.F. All authors have read and agreed to the published version of the manuscript.

Funding: This research received no external funding.

Acknowledgments: The authors are grateful to Franklin Electric srl for his valuable support in the experimental activities.

Conflicts of Interest: The authors declare no conflict of interest.

References

1. Sonawat, A.; Kim, S.; Ma, S.B.; Kim, S.J.; Lee, J.B.; Yu, M.S.; Kim, J.H. Investigation of unsteady pressure fluctuations and methods for its suppression for a double suction centrifugal pump. *Energy* **2022**, *252*, 124020. [CrossRef]
2. Capurso, T.; Bergamini, L.; Torresi, M. Performance analysis of double suction centrifugal pumps with a novel impeller configuration. *Energy Convers. Manag.* **2022**, *14*, 100227. [CrossRef]
3. Michaelides, K.V.; Tourlidakis, A.; Elder, R.L. Use of CFD for the three-dimensional hydrodynamic design of vertical diffuser pumps. In *Advances of CFD in Fluid Machinery Design*; Elder, R.L., Tourlidakis, A., Yates, M., Eds.; Professional Engineering Publishing-Wiley and Sons: Bury St Edmunds, UK, 2002; pp. 129–148.
4. Kaupert, K.A. An Evaluation of Impeller Blade Torque During an Impeller–Diffuser Interaction. *J. Fluids Eng.* **2004**, *126*, 960–965. [CrossRef]
5. Roclawski, H.; Hellmann, D.H. Rotor-Stator-Interaction of a Radial Centrifugal Pump Stage with Minimum Stage Diameter. In Proceedings of the 4th WSEAS International Conference on Fluid Mechanics and Aerodynamics, Elounda, Greece, 21–23 August 2006; pp. 301–308.
6. Yang, C.; Cheng, X. Numerical simulation of the three-dimensional flow in a multistage centrifugal pump based on integral modeling. In Proceedings of the Power and Energy Engineering Conference, Wuhan, China, 27–31 March 2009; pp. 1–5. [CrossRef]
7. Zhou, L.; Shi, W.; Lu, W.; Hu, B.; Wu, S. Numerical Investigations and Performance Experiments of a Deep-Well Centrifugal Pump with Different Diffusers. *J. Fluids Eng.* **2012**, *134*, 071102. [CrossRef]
8. Shi, W.; Zhou, L.; Lu, W.; Pei, B.; Lang, T. Numerical Prediction and Performance Experiment in a Deep-well Centrifugal Pump with Different Impeller Outlet Width. *Chin. J. Mech. Eng.* **2013**, *26*, 46–52. [CrossRef]
9. Huang, S.; Islam, M.F.; Liu, P. CFD Analysis and Experimental Verification of Multi-stage Centrifugal Pump with Multi-outlet options. *Appl. Mech. Mater.* **2013**, *331*, 94–97. [CrossRef]
10. Wang, W.J.; Li, G.D.; Wang, Y.; Cui, Y.R.; Yin, G.; Peng, S. Numerical simulation and performance prediction in multi-stage submersible centrifugal pump. *IOP Conf. Ser. Mater. Sci. Eng.* **2013**, *52*, 032001. [CrossRef]
11. Rakibuzzaman, R.; Suh, S.H.; Kim, K.W.; Kim, H.H.; Cho, M.T.; Yoon, I.S. A Study on Multistage Centrifugal Pump Performance Characteristics for Variable Speed Drive System. *Procedia Eng.* **2015**, *105*, 270–275. [CrossRef]
12. Lee, J.; Mosfeghi, M.; Hur, N.; Yoon, I.S. Flow analysis in a return channel of a multi-stage centrifugal pump. *J. Mech. Sci. Technol.* **2016**, *30*, 3993–4000. [CrossRef]
13. Li, W.; Jang, X.; Pang, Q.; Zhou, L.; Wang, W. Numerical simulation and performance analysis of a four-stage centrifugal pump. *SAGE Adv. Mech. Eng.* **2016**, *8*, 1–8. [CrossRef]
14. Fontana, F.; Masi, M. CFD modelling to aid the design of steel sheet multistage pumps. In Proceedings of the 29th International Conference on Efficiency, Cost, Optimization, Simulation and Environmental Impact of Energy Systems, Portoroz, Slovenia, 19–23 June 2016.
15. Zhu, J.; Banjar, H.; Xia, Z.; Zhang, H.Q. CFD simulation and experimental study of oil viscosity effect on multi-stage electrical submersible pump (ESP) performance. *J. Petrol. Sci. Eng.* **2016**, *146*, 735–745. [CrossRef]
16. Wang, C.; Shi, W.; Wanga, X.; Jiang, X.; Yang, Y.; Li, W.; Zhou, L. Optimal design of multistage centrifugal pump based on the combined energy loss model and computational fluid dynamics. *Appl. Energy* **2017**, *187*, 10–26. [CrossRef]
17. Zhu, J.; Zhou, H.; Zhang, J.; Zhang, H.Q. A numerical study on flow patterns inside an electrical submersible pump (ESP) and comparison with visualization experiments. *J. Petrol. Sci. Eng.* **2019**, *173*, 339–350. [CrossRef]
18. Valdés, J.P.; Becerra, D.; Rozo, D.; Cediel, A.; Torres, F.; Asuaje, M.; Ratkovich, N. Comparative analysis of an electrical submersible pump's performance handling viscous Newtonian and non-Newtonian fluids through experimental and CFD approaches. *J. Petrol. Sci. Eng.* **2020**, *187*, 106749. [CrossRef]
19. Yan, S.; Luo, X.; Sun, S.; Zhang, L.; Chen, S.; Feng, J. Influence of inlet gas volume fraction on energy conversion characteristics of multistage electric submersible pump. *J. Petrol. Sci. Eng.* **2021**, *207*, 109164. [CrossRef]

20. Kang, Y.; Su, Q.; Liu, S. On the axial thrust and hydraulic performance of a multistage lifting pump for deep-sea mining. *Ocean. Eng.* **2022**, *265*, 112534. [CrossRef]
21. Bai, L.; Yang, Y.; Zhou, L.; Li, Y.; Xiao, Y.; Shi, W. Optimal design and performance improvement of an electric submersible pump impeller based on Taguchi approach. *Energy* **2022**, *252*, 124032. [CrossRef]
22. Ha, T.W.; Lee, Y.B.; Kim, C.H. Leakage and rotordynamic analysis of a high pressure floating ring seal in the turbo pump unit of a liquid rocket engine. *Tribol. Int.* **2002**, *35*, 153–161. [CrossRef]
23. Adami, P.; Della Gatta, S.; Martelli, F.; Bertolazzi, L.; Maestri, D.; Marenco, G.; Piva, A. Multistage centrifugal-pumps: Assessment of a mixing plane method for CFD analysis. In Proceedings of the 60° Congresso Nazionale ATI, Roma, Italy, 13–15 September 2005.
24. Salvadori, S.; Marini, A.; Martelli, F. Methodology for the Residual Axial Thrust Evaluation in Multistage Centrifugal Pumps. *Eng. Appl. Comput. Fluid Mech.* **2012**, *6*, 271–284. [CrossRef]
25. Gülich, J.F. *Centrifugal Pumps*, 2nd ed.; Springer: Berlin, Germany, 2010. [CrossRef]
26. Fontana, F. Estimation of the head loss in the annular chamber of multistage centrifugal pumps featuring a compact design. In Proceedings of the 1st Global Power and Propulsion Forum GPPF 2017, Zurich, Switzerland, 16–18 January 2017.
27. Fontana, F. Design and Analysis of Compact-Design Rotodynamic Multistage Pumps. Ph.D. Thesis, University of Padova, Padua, Italy, 15 January 2018. (In Italian).
28. Zhou, L.; Shi, W.; Li, W.; Agarwal, R. Numerical and Experimental Study of Axial Force and Hydraulic Performance in a Deep-Well Centrifugal Pump with Different Impeller Rear Shroud Radius. *J. Fluids Eng.* **2013**, *135*, 104501. [CrossRef]